DUET: Improving Inertial-based Odometry via Deep IMU Online Calibration

Huakun Liu, Xin Wei, Monica Perusquía-Hernández,
Naoya Isoyama, Hideaki Uchiyama, and Kiyoshi Kiyokawa

***Abstract*—This paper presents a deep data-driven inertial measurement unit (IMU) online calibration (DUET) method that can compensate for the run-time errors of the accelerometer and gyroscope to improve inertial-based odometry. We design a differential error learning strategy based on the kinematic motion model to train the sensor error compensation model. This strategy allows our method to learn IMU sensor errors, such as scale factors, axis-misalignment, and biases, solely from displacement and orientation increments given by external tracking systems. Then during the odometry computation, the trained model leverages the past inertial data to mitigate the sensor errors and thus reduces the integration errors to reflect the odometry state. The experiments conducted on two public visual-inertial datasets show an average of 20% improvement in the position estimation accuracy of visual-inertial odometry, which is comparable to existing learning-based methods with lower operational complexity.**

***Index Terms*—Inertial sensors, calibration, localization, deep learning.**

I. Introduction

ODOMETRY is a process to track the position and orientation of the tracking target relative to its starting pose in a 3D space. It is a fundamental element for various applications in health care [1], [2] and virtual/augmented reality [3]. Recent odometry methods are mainly inertial-based, such as visual-inertial odometry (VIO) [4] and inertial-only odometry (IO) [5]. The essential component of inertial-based odometry is the microelectromechanical system (MEMS) inertial measurement unit (IMU). It consists of an accelerometer and a gyroscope that measure accelerations and angular velocities to provide continuous and high-frequency tracking.

VIO uses a lightweight camera to capture visual data and a low-cost and small-size MEMS IMU to measure inertial data. By fusing the visual data and inertial data, it has achieved centimeter-level accuracy in 6 degrees of freedom (DoF) odometry [6]. However, in challenging scenes such as extreme brightness and dynamic environments, its accuracy is degraded to meter-level when visual odometry fails, and the odometry relies solely on IMU measurement integration [7]. IO is seen as the most compact method because it utilizes only a small MEMS IMU and has lower computational complexity and higher robustness to surrounding changes. However, it suffers from low accuracy due to the rapid accumulation of various IMU errors during the integration [5]. The MEMS IMU errors include scale factors, axis-misalignment, zero-biases, and noise [8]. During the integration process, these errors explode exponentially with time. As a result, IO is unreliable even for a few seconds.

IMU calibration is a method to diminish these problems. It is a process to measure and compensate for gyroscope and accelerometer errors before or during odometry computation to mitigate the negative impact of IMU errors on inertial-based odometry results. Traditional offline calibration methods, such as the multi-position method, can identify the unknown error parameters by optimization algorithms with external reference information [9]–[12]. However, they are not applicable to handling high non-linear and time-varying errors. Online calibration methods, such as sensor fusion and filtering-based methods [13], can estimate and compensate for run-time IMU errors by fusing multi-sensor and using additional information. It is capable of handling poor offline calibration and time-varying sensor errors, thus improving the odometry results at run-time. However, the performance is highly dependent on the fused sensors' reliability. For example, in visually challenging scenarios such as dark environment, VIO no longer applies to error compensation [7].

Recent data-driven online calibration methods, such as Denoising IMU Gyro (DIG) [14] and Temporal Convolutional Network Denoising IMU Gyro (TCN-DIG) [15], use supervised learning to train a calibration model and then directly output correction terms, that is, biases and noise, by inputting the run-time inertial data. These learning-based standalone systems are capable of calibrating complex run-time sensor errors from only IMU sequences and have demonstrated superior performance over traditional filtering-based approaches [16]. In inertial-based odometry scenarios, it is feasible to learn an IMU calibration model in the training process using the dynamic positions and orientations captured by high-precision tracking systems such as the laser tracker and the optical tracker [17]–[20]. However, these methods require additional sensors and assumption-based processed data such as derived accelerations based on the constant-velocity assumption in addition to the tracking system. This increases the operational complexity and limits the scenarios in which these data-driven methods can be applied. Currently, there is still a lack of a simple yet universal data-driven calibration model and learning strategy for robust inertial-based odometry.

The main challenge arises from the module that calibrates the accelerometers. On the one hand, an accelerometer senses not only its linear acceleration but also the local gravity. As a

H. Liu, X. Wei, M. Perusquía-Hernández, H. Uchiyama, and K. Kiyokawa are with the Cybernetics and Reality Engineering Laboratory, Nara Institute of Science and Technology, Nara, Japan–https://carelab.info.

N. Isoyama is with the Amusing Interaction Design Laboratory, Otsuma Women's University, Tokyo, Japan–https://www.sis.otsuma.ac.jp/aid-lab.

result, the presence of a standard gravity value leads to larger noise densities in accelerometers compared to gyroscopes. This increases the difficulty of predicting its correction term, i.e., bias and noise [21]. On the other hand, tracking systems such as laser and optical trackers only capture high-precision positions and orientations. Training the gyroscope calibration model from the ground truth orientations is feasible because the orientation can be obtained by directly integrating the angular velocity. However, training the accelerometer calibration model based on ground truth positions is not straightforwardly feasible unless ground truth velocities or accelerations are also provided [19].

Most data-driven IMU calibration studies have focused on learning the calibration model using extra sensors and assumption-based processed data, in addition to high-precision tracking systems. However, in this work, we propose to learn sensor errors solely from high-precision orientations and positions without additional sensors, which allows data-driven calibration to be applied to a broader range of scenarios. This obtained performance is attributed to a loss function designed based on the kinematic motion model. Moreover, we conducted the first comprehensive experiments on datasets covering multiple scenarios using different metrics to delve into the impact of data-driven calibration methods on IO and VIO. Our main contributions are as follows:

- A deep data-driven IMU calibration method based on two connected dilated convolution networks for calibrating dynamic gyroscope and accelerometer data simultaneously. With this, we overcome the limitation of using separate models to calibrate gyroscope and accelerometer data, respectively.
- A loss function based on the kinematic motion model for learning the errors using solely ground truth positions and orientations. This simplifies the learning process and improves the applicability of data-driven IMU calibration methods.
- A first thorough analysis through extensive experiments on sensor readings, velocity, orientation, and position estimates to evaluate the impact of the data-driven IMU calibration method on the 6-DoF inertial odometry and visual-inertial odometry. The results reveal the effectiveness of data-driven calibration on reducing the error accumulation rate of IO and improving the robustness of VIO.

The rest of the paper is organized as follows. In Section II, we introduce the related work, which includes traditional and state-of-the-art data-driven gyroscope and accelerometer calibration methods. In Section III, we introduce our deep IMU calibration method. Finally, Section IV provides the experimental results, and the conclusions and future directions are presented in Section V.

II. Related Work

Deep learning has provided new possibilities for unimodal position estimation from IMU. For instance, it is used to extract latent features from IMU signals to estimate the velocity [5], orientation [22], and displacement [23]–[26]. These methods have seen great success in 6-DoF IO, owing to avoiding the error accumulation caused by the integration process. Additionally, using data-driven deep learning to calibrate run-time gyroscopes and accelerometers has become popular [27]. This is because introducing deep learning decreases human intervention, facilitates the realization of autonomous online calibration systems, and is well coupled with inertial-based odometry [8].

A. Data-driven Gyroscope Calibration

In [28], the first long short-term memory (LSTM)-recurrent neural network (RNN)-based denoising method was proposed to denoise IMU gyroscope signals. Compared to autoregressive and moving average models, the standard deviation of denoised signals decreased by up to 42.4% with deep learning. In [16], learning-based OriNet was proposed to estimate the 3D orientation with a genetic bias calibration algorithm. The orientation estimation in real scenarios was improved by 72% compared to the complementary filter and 89% compared to Madgwick filter. Consequently, there is a growing interest in applying learning-based methods to improve inertial-based odometry. Brossard *et al.* [14] proposed a convolutional neural network (CNN) to predict the run-time gyroscope correction term, i.e., zero bias and noise, and to find the optimal coefficients of scale factor and axis-misalignment during training from measured accelerometer and gyroscope readings. Then, Huang *et al.* [15] used a temporal convolutional network to further improve the performance of the gyroscope online calibration. They showed that the orientation estimated from the calibrated gyroscope data could be used to improve the accuracy of the VIO position estimation. To solve the low generalizability problem of data-driven denoising models, Yao [29] proposed a few-shot domain adaptation gyroscope calibration method that consists of an embedding module, restructor module, and generator module.

B. Data-driven Accelerometer Calibration

Engelsman and Klein [21] implemented three learning algorithms and one machine learning method, including unidirectional bi-layer LSTM, bi-directional one-layer RNN, bidirectional one-layer gated recurrent unit (GRU), and k-nearest neighbor, to calibrate the accelerometer. The evaluation of a simulated dataset and static accelerometer data showed that data-driven accelerometer calibration achieves a 60% noise reduction and 20% improvement in stationary course alignment compared to traditional methods.

Our basic network structure is similar to the aforementioned data-driven gyroscope or accelerometer calibration methods, which are based on convolutional neural networks. However, instead of calibrating only one component of an IMU, we simultaneously calibrate the gyroscope and accelerometer.

C. Data-driven IMU Calibration

Chen *et al.* [17] used a convolutional neural network to reduce errors from both the accelerometer and gyroscope in a laboratory environment. As a reference, the ground truth acceleration and angular velocity data were generated from a well-designed linear motion stage and a rotary motor. Zhang *et al.* [18] trained an RNN to calibrate the run-time gyroscope and accelerometer. Additional high-quality sensors and sensor fusion algorithms provide ground truth orientations, velocities, and positions to train the calibration model. Similarly, Steinbrener *et al.* [19] proposed LSTM-based and Transformer-based methods to output calibrated IMU measurements for real-time 6-DoF pose estimation. The ground truth velocities are computed from positions based on the assumption that velocities are constant between two consecutive frames. Recently, Buchanan *et al.* [20] proposed to train both LSTM and Transformer from the optimized ground truth biases of target IMU to learn and compensate for the bias. They showed that fusing the data-driven bias compensation model with VIO reduced the drift rate by an average of 15%.

Our objective is similar to these studies to build the calibration model from high-precision dynamic motion data and then mitigate the sensor errors at run-time. Nevertheless, these methods are forced to rely on external sensors and complex setups to learn the model. In contrast, our proposed general learning strategy keeps us from relying on these.

III. Deep IMU Online Calibration (DUET)

In this section, we first present an IMU sensor error model and a kinematic motion model used in inertial-based odometry, followed by our deep IMU calibration network structure and the loss function.

A. Preliminaries

Sensor error model A MEMS IMU consists of an accelerometer and a gyroscope that measures the acceleration $\boldsymbol{a}$ and the angular velocity $\boldsymbol{\omega}$ of the carrier. However, the measurement contains not only the true $\boldsymbol{a}$ and $\boldsymbol{\omega}$, but also other error terms.

Given a three-axis strapdown accelerometer and gyroscope, a commonly used error model is established as follows [8]:

$$\tilde{\boldsymbol{u}} = (\boldsymbol{S} + \boldsymbol{N})\boldsymbol{u} + \boldsymbol{b} + \boldsymbol{n}, \tag{1}$$

where $\tilde{\boldsymbol{u}} \in \mathbb{R}^3$ and $\boldsymbol{u} \in \mathbb{R}^3$ denote the measurement output of an IMU and the true acceleration or angular velocity, respectively. $\boldsymbol{S} \in \mathbb{R}^{3\times3}$ is the scale factor that refers to the ratio between the output quantity and the input quantity. $\boldsymbol{N} \in \mathbb{R}^{3\times3}$ denotes the axis-misalignment error results from the non-orthogonality between each axis. $\boldsymbol{b} \in \mathbb{R}^3$ is the so-called zero-bias. It is the output value of the accelerometer or gyroscope when the measured physical quantity is equal to zero. $\boldsymbol{n} \in \mathbb{R}^3$ is commonly assumed to be the high-frequency random sensor white noise that follows the zero-mean Gaussian distribution. Their matrix elements are defined as follows:

$$\begin{aligned} \boldsymbol{S} &= \begin{bmatrix} s_x & 0 & 0 \\ 0 & s_y & 0 \\ 0 & 0 & s_z \end{bmatrix}, \quad \boldsymbol{b} = \begin{bmatrix} b_x \\ b_y \\ b_z \end{bmatrix}, \\ \boldsymbol{N} &= \begin{bmatrix} 0 & \gamma_{xy} & \gamma_{xz} \\ \gamma_{yx} & 0 & \gamma_{yz} \\ \gamma_{zx} & \gamma_{zy} & 0 \end{bmatrix}, \quad \boldsymbol{n} = \begin{bmatrix} n_x \\ n_y \\ n_z \end{bmatrix}. \end{aligned} \tag{2}$$

Kinematic motion model Inertial and visual-inertial odometry calculate the trajectory from the acceleration and angular velocity obtained from an IMU using the kinematic motion model. The core processing is to rotate the acceleration from the IMU frame to a fixed global frame and then accumulate it to compute the velocity and the moving distance.

Given the angular velocity $\boldsymbol{\omega}$ obtained from a gyroscope, the special orthogonal rotation matrix in 3D space $\boldsymbol{R} \in SO(3)$ that maps from IMU frame to global frame at time step i can be expressed as follows:

$$\boldsymbol{R}_i = \boldsymbol{R}_{i-1} \exp(\boldsymbol{\omega}_{i-1}\Delta t), \tag{3}$$

where $\exp(\cdot)$ is the $SO(3)$ exponential map and Δt is the time interval of two consecutive frames. The velocity $\boldsymbol{v}$ in the global frame is then calculated by rotating the measured acceleration $\boldsymbol{a}$ and removing the local gravity $\boldsymbol{g}$,

$$\boldsymbol{v}_i = \boldsymbol{v}_{i-1} + (\boldsymbol{R}_{i-1}\boldsymbol{a}_{i-1} + \boldsymbol{g})\Delta t, \quad \boldsymbol{g} = \begin{bmatrix} 0 \\ 0 \\ -g \end{bmatrix}. \tag{4}$$

Finally, the position in the fixed global frame is calculated as follows:

$$\boldsymbol{p}_i = \boldsymbol{p}_{i-1} + \boldsymbol{v}_{i-1}\Delta t + \frac{1}{2}(\boldsymbol{R}_{i-1}\boldsymbol{a}_{i-1} + \boldsymbol{g})\Delta t^2. \tag{5}$$

B. Problem Modeling

According to the sensor error model in (1), the value $\boldsymbol{u}_i$ of an IMU accelerometer or gyroscope at time step i can be expressed as follows:

$$\boldsymbol{u}_i = (\boldsymbol{S} + \boldsymbol{N})^{-1} \left(\tilde{\boldsymbol{u}}_i - (\boldsymbol{b}_i + \boldsymbol{n}_i)\right). \tag{6}$$

To simplify the problem, we denote $(\boldsymbol{S}+\boldsymbol{N})^{-1}$ and $(\boldsymbol{b}_i+\boldsymbol{n}_i)$ in (6) by $\boldsymbol{C} \in \mathbb{R}^{3\times3}$ and $\boldsymbol{\varepsilon}_i \in \mathbb{R}^3$, respectively. $\boldsymbol{C}$ contains both the scale factor and axis-misalignment. $\boldsymbol{\varepsilon}_i$ is the correction term that contains zero bias and noise. They are expressed as follows:

$$\boldsymbol{C} = \begin{bmatrix} s_x & \gamma_{xy} & \gamma_{xz} \\ \gamma_{yx} & s_y & \gamma_{yz} \\ \gamma_{zx} & \gamma_{zy} & s_z \end{bmatrix}^{-1}, \quad \boldsymbol{\varepsilon}_i = \begin{bmatrix} b_x + n_x \\ b_y + n_y \\ b_z + n_z \end{bmatrix}. \tag{7}$$

Then, we have

$$\boldsymbol{u}_i = \boldsymbol{C}(\tilde{\boldsymbol{u}}_i - \boldsymbol{\varepsilon}_i). \tag{8}$$

In this paper, we aim to improve the IMU data reliability by learning, predicting, and compensating for $\boldsymbol{C}$ and $\boldsymbol{\varepsilon}_i$ using a deep neural network.

C. Network Structure

Our network structure is based on the dilated convolutional neural network [30]. A dilated CNN is a type of CNN that uses dilated convolutions to exponentially expand the receptive field with few memory consumption and efficient computation. The dilated convolutions enable the network to maintain the temporal property of the data and capture long-range contextual information, making it suitable for time-series data. This network is widely used for data-driven calibration because it is lightweight and has no loss of accuracy compared to recurrent neural networks [14], [15].

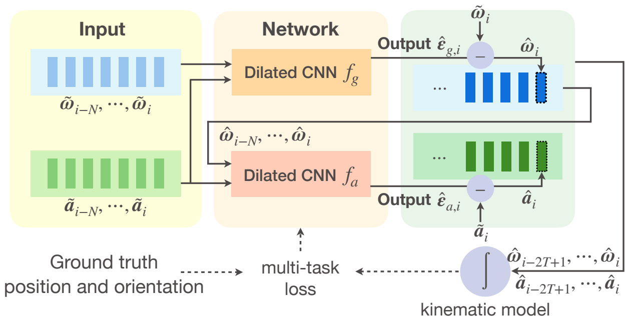
Input
Network
Dilated CNN f_g
Dilated CNN f_a
Output $\hat{\varepsilon}_{g,i}$
Output $\hat{\varepsilon}_{a,i}$
$\tilde{\omega}_{i-N}, \cdots, \tilde{\omega}_i$
$\tilde{a}_{i-N}, \cdots, \tilde{a}_i$
$\hat{\omega}_{i-N}, \cdots, \hat{\omega}_i$
Ground truth position and orientation
multi-task loss
kinematic model
$\hat{\omega}_{i-2T+1}, \cdots, \hat{\omega}_i$
$\hat{a}_{i-2T+1}, \cdots, \hat{a}_i$

(a) Flowchart of building the calibration model.

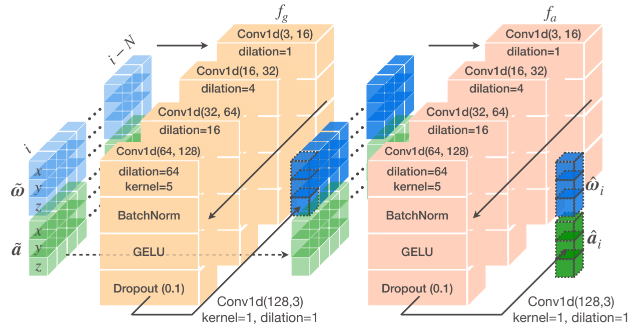

(b) Network architecture.

Fig. 1. The flowchart of building the calibration model and the network architecture for calibrating run-time gyroscope and accelerometer measurements. The first dilated convolutional network inputs $N+1$ frames raw IMU measurements and outputs current frame calibrated angular velocity. Then the second dilated convolutional network inputs $N+1$ frames calibrated angular velocities and raw accelerations then outputs the current frame calibrated acceleration. $N = 340$ is determined by the network architecture. When training the calibration model, the ground truth orientations and positions are used to compute the loss with inferred values from calibrated angular velocities and accelerations.

As shown in Figure 1, we define the network as predicting the correction term $\hat{\varepsilon}_{a,i}$ and $\hat{\varepsilon}_{g,i}$ for the accelerometer and the gyroscope from uncalibrated IMU data. In particular, we leverage the current frame and past N frames of uncalibrated 3-axis accelerations $(\tilde{\boldsymbol{a}}_{i-N}, \cdots, \tilde{\boldsymbol{a}}_i)$ and 3-axis angular velocities $(\tilde{\boldsymbol{\omega}}_{i-N}, \cdots, \tilde{\boldsymbol{\omega}}_i)$ to predict the correction term $\hat{\varepsilon}_{g,i}$. In addition, we optimize the multiplier $\boldsymbol{C}_g$ for the angular velocity $\boldsymbol{\omega}_i$ during training. The neural network that predicts $\hat{\varepsilon}_{g,i}$ at time step i can be expressed as follows:

$$\hat{\varepsilon}_{g,i} = f_g((\tilde{\boldsymbol{a}}_{i-N}, \tilde{\boldsymbol{\omega}}_{i-N}), \cdots, (\tilde{\boldsymbol{a}}_i, \tilde{\boldsymbol{\omega}}_i)), \tag{9}$$

where $f_g(\cdot)$ is the function defined by a dilated convolutional neural network. Then, the calibrated angular velocity $\hat{\boldsymbol{\omega}}_i$ is computed by

$$\hat{\boldsymbol{\omega}}_i = \hat{\boldsymbol{C}}_g(\tilde{\boldsymbol{\omega}}_i - \hat{\varepsilon}_{g,i}). \tag{10}$$

After obtaining calibrated angular velocities, we pass these values with uncalibrated accelerations into the second dilated neural network to optimize the multiplier $\boldsymbol{C}_a$ during training and predict the acceleration correction term $\hat{\varepsilon}_{a,i}$, which is defined as follows:

$$\hat{\varepsilon}_{a,i} = f_a((\tilde{\boldsymbol{a}}_{i-N}, \hat{\boldsymbol{\omega}}_{i-N}), \cdots, (\tilde{\boldsymbol{a}}_i, \hat{\boldsymbol{\omega}}_i)). \tag{11}$$

Similarly, the calibrated acceleration $\hat{\boldsymbol{a}}_i$ is computed by

$$\hat{\boldsymbol{a}}_i = \hat{\boldsymbol{C}}_a(\tilde{\boldsymbol{a}}_i - \hat{\varepsilon}_{a,i}). \tag{12}$$

The network architecture is presented in Figure 1b. Note that the input of $f_a(\cdot)$ consists of uncalibrated accelerations and calibrated angular velocities, which are used to connect $f_a(\cdot)$ and $f_g(\cdot)$. Furthermore, from (5), the accurate inferred position depends on both angular velocity and acceleration. Thus, it is reasonable to learn the acceleration error from calibrated angular velocities, which also mitigates the impact of gyroscope errors.

D. Loss Function

The most straightforward way to train the model is to minimize the loss between the predicted and target ground truth acceleration and angular velocity. However, given high-precision positions and orientations, acquiring the dynamic ground truth IMU data at a high IMU frequency (200 Hz or more) is not feasible in practice. This is because the derivative process of high-precision positions suffers from a jitter problem [19] (see Section IV-D2 for more details). Therefore, solely using ground truth positions and orientations for learning is a preferred solution.

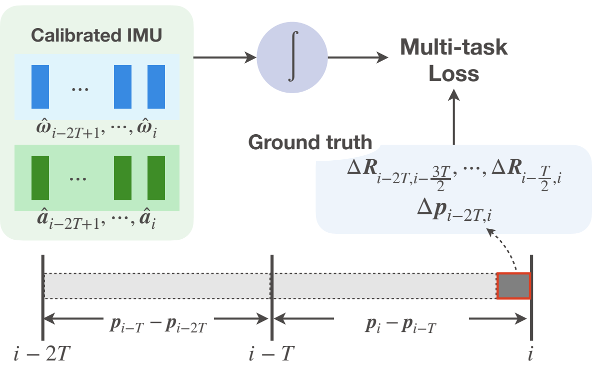
Calibrated IMU
$\hat{\omega}_{i-2T+1}, \cdots, \hat{\omega}_i$
$\hat{a}_{i-2T+1}, \cdots, \hat{a}_i$
Multi-task Loss
Ground truth
$\Delta R_{i-2T,i-\frac{3T}{2}}, \cdots, \Delta R_{i-\frac{T}{2},i}$
$\Delta p_{i-2T,i}$
$p_{i-T} - p_{i-2T}$
$p_i - p_{i-T}$
$i-2T$
$i-T$
i

Fig. 2. Schematic diagram of the proposed loss function. The target is to minimize: 1) the residuals between the ground truth displacement difference and the calibrated displacement difference with the condition of T window size for each displacement; 2) the difference between the accumulated orientation from calibrated angular velocity and the ground truth orientation over $\frac{T}{2}$ windows.

We first consider learning accelerometer errors from positions. From the position inference function (5), the displacement between two consecutive frames, i.e., with the condition that the window size equals to 1, can be expressed as:

$$\begin{aligned}\boldsymbol{p}_i - \boldsymbol{p}_{i-1} &= \boldsymbol{v}_{i-1}\Delta t + \frac{1}{2}(\boldsymbol{R}_{i-1}\boldsymbol{a}_{i-1} + \boldsymbol{g})\Delta t^2 \qquad (13)\\ &= \boldsymbol{v}_{i-1}\Delta t + \frac{1}{2}\boldsymbol{a}^W_{i-1}\Delta t^2, \qquad (14)\end{aligned}$$

where

$$\boldsymbol{a}^W_{i-1} = \boldsymbol{R}_{i-1}\boldsymbol{a}_{i-1} + \boldsymbol{g} \tag{15}$$

is the linear acceleration in the fixed world frame at time step $i-1$. However, the initial velocity $\boldsymbol{v}_{i-1}$ in (13) is not available in practice, especially when the tracked object does not move from stationary. Thus, to remove the effect of the uncertain

$\boldsymbol{v}_{i-1}$, we consider a consecutive displacement between $\boldsymbol{p}_{i-2}$ and $\boldsymbol{p}_{i-1}$ as

$$\boldsymbol{p}_{i-1} - \boldsymbol{p}_{i-2} = \boldsymbol{v}_{i-2}\Delta t + \frac{1}{2}\boldsymbol{a}^{W}_{i-2}\Delta t^2. \quad (16)$$

Then, according to the velocity inference function (4), equation (13) can be further formulated as:

$$\begin{aligned}\boldsymbol{p}_{i} - \boldsymbol{p}_{i-1} &= (\boldsymbol{v}_{i-2} + \boldsymbol{a}^{W}_{i-2}\Delta t)\Delta t + \frac{1}{2}\boldsymbol{a}^{W}_{i-1}\Delta t^2 \\ &= \boldsymbol{v}_{i-2}\Delta t + \boldsymbol{a}^{W}_{i-2}\Delta t^2 + \frac{1}{2}\boldsymbol{a}^{W}_{i-1}\Delta t^2. \quad (17)\end{aligned}$$

We define $\Delta\boldsymbol{p}_{i-2,i}$ as the difference of displacement $\boldsymbol{p}_i - \boldsymbol{p}_{i-1}$ and $\boldsymbol{p}_{i-1} - \boldsymbol{p}_{i-2}$, that is,

$$\begin{aligned}\Delta\boldsymbol{p}_{i-2,i} &= (\boldsymbol{p}_i - \boldsymbol{p}_{i-1}) - (\boldsymbol{p}_{i-1} - \boldsymbol{p}_{i-2}) \\ &= \frac{1}{2}\boldsymbol{a}^{W}_{i-2}\Delta t^2 + \frac{1}{2}\boldsymbol{a}^{W}_{i-1}\Delta t^2. \quad (18)\end{aligned}$$

Thus, the displacement difference can be expressed as a function of the linear acceleration in the fixed world frame. However, using (18) still suffers from high-frequency position jitters. We thus expand the window size of each displacement to T and calculate the cumulative difference over $2T$ windows. This allows for attenuating position jitter effects in the calculation by enlarging the displacement difference. Similar to the calculation of $\Delta\boldsymbol{p}_{i-2,i}$, we derive that $\Delta\boldsymbol{p}_{i-2T,i}$ can be expressed as only related to the linear acceleration within the corresponding period as:

$$\begin{aligned}\Delta\boldsymbol{p}_{i-2T,i} &= (\boldsymbol{p}_i - \boldsymbol{p}_{i-T}) - (\boldsymbol{p}_{i-T} - \boldsymbol{p}_{i-2T}) \\ &= \sum_{j=1}^{T} j\boldsymbol{a}^{W}_{i-2T+j-1}\Delta t^2 + \sum_{j=1}^{T-1}(T-j)\boldsymbol{a}^{W}_{i-T+j-1}\Delta t^2 \\ &\quad + \frac{1}{2}\sum_{j=0}^{T-1}(\boldsymbol{a}^{W}_{i-T+j} - \boldsymbol{a}^{W}_{i-2T+j})\Delta t^2, \quad (19)\end{aligned}$$

where T is the window size of each displacement. $\boldsymbol{a}^{W}_{i+j}$ is the linear acceleration in the fixed world frame at time step $i+j$ and computed as:

$$\boldsymbol{a}^{W}_{i+j} = \boldsymbol{R}_{i+j}\boldsymbol{a}_{i+j} + \boldsymbol{g}. \quad (20)$$

Figure 2 represents the schematic diagram of the loss function. We define the loss function based on (19) and (20) as:

$$\mathcal{L}_1\Big((\boldsymbol{p}, \boldsymbol{R}), \hat{\boldsymbol{a}}\Big) = \sum_i \rho(\Delta\boldsymbol{p}_{i-2T,i} - \Delta\hat{\boldsymbol{p}}_{i-2T,i}), \quad (21)$$

where $\Delta\boldsymbol{p}_{i-2T,i}$ is computed from ground truth positions, $\Delta\hat{\boldsymbol{p}}_{i-2T,i}$ is calculated from the computed acceleration $(\hat{\boldsymbol{a}}_{i-2T}, \cdots, \hat{\boldsymbol{a}}_i)$ through (12), (19), and (20), and $\rho(\cdot)$ is the Huber loss function [31].

In order to train the model for gyroscope calibration, we minimize the accumulated orientation error within every $T/2$ windows as:

$$\mathcal{L}_2(\boldsymbol{R}, \hat{\boldsymbol{\omega}}) = \sum_i \rho\left(\log_{SO3}\left(\Delta\boldsymbol{R}_{i,i+\frac{T}{2}}\Delta\hat{\boldsymbol{R}}^{-1}_{i,i+\frac{T}{2}}\right)\right) \quad (22)$$

$$\Delta\boldsymbol{R}_{i,i+\frac{T}{2}} = \boldsymbol{R}_i^{-1}\boldsymbol{R}_{i+\frac{T}{2}} \quad (23)$$

$$\Delta\hat{\boldsymbol{R}}_{i,i+\frac{T}{2}} = \prod_{j=i}^{i+\frac{T}{2}-1} \exp_{SO3}(\hat{\boldsymbol{\omega}}_j\Delta t) \quad (24)$$

where $\log_{SO3}(\cdot)$ is the $SO(3)$ logarithm map. Note that the output of the first layer network is also used as the input of the second layer network. Thus, we set a larger error calculation frequency of gyroscope than that of accelerometer, as every $\frac{T}{2}$ windows against every $2T$ windows. This allows for a faster convergence of the first layer network for calibrating gyroscope and further aided in the training of the second layer network used to calibrate the accelerometer.

Finally, we use the sum of $\mathcal{L}_1$ and $\mathcal{L}_2$ to jointly train the network:

$$\mathcal{L} = w_1\mathcal{L}_1\Big((\boldsymbol{p}, \boldsymbol{R}), \hat{\boldsymbol{a}}\Big) + w_2\mathcal{L}_2(\boldsymbol{R}, \hat{\boldsymbol{\omega}}). \quad (25)$$

The computational complexity of $\mathcal{L}$ is $O(n)$, however, in practice, the computation time depends more on the window size T because of the matrix multiplications when calculating the accumulated orientation within each window. In our experiments, we analyzed the impact of T on the training time, see Section IV-F for details. Furthermore, for balancing the two loss terms, we adopt multi-task training strategy [32] to adapt the weights as

$$\begin{aligned}\mathcal{L} = &\frac{1}{2c_1}\mathcal{L}_1\Big((\boldsymbol{p}, \boldsymbol{R}), \hat{\boldsymbol{a}}\Big) + \ln(1 + c_1^2) \\ &+ \frac{1}{2c_2}\mathcal{L}_2(\boldsymbol{R}, \hat{\boldsymbol{\omega}}) + \ln(1 + c_2^2), \quad (26)\end{aligned}$$

where c_1 and c_2 are parameters optimized during training. The objective of (26) is to train the calibration model by minimizing the adaptive weighted sum of the accumulated displacement error and orientation error.

IV. Experiments

In this section, we present two experiments to evaluate the proposed method. In the first experiment, we analyze the direct output of our model, i.e., the predicted sensor error, and compare it with the raw sensor errors. In the second experiment, we evaluate the proposed method in terms of orientation, velocity, and position estimation by comparing it with existing methods. Additionally, we offer two discussions on the generalization issue of the data-driven method and the hyperparameter T. In the first discussion, we explore the impact of bias changes on the model performance by analyzing the correlation between biases and evaluation results. Then, we performed further experimental validation to clarify these findings. In the second discussion, we analyze the impact of the T on the model performance and training time. Then, we emphasize a few important points for setting a proper T.

A. Datasets

1) EuRoC: EuRoC [33] is one of the most used visual-inertial datasets. The dataset contains various sequences collected by a micro aerial vehicle (MAV). The angular velocity and specific force were measured using an uncalibrated ADIS16448 IMU at 200 Hz. Ground truth positions were recorded at 20 Hz using a Leica Nova MS50 laser tracker.

For sequences collected in a Vicon room, the 6D pose of the MAV was recorded by the Vicon motion capture system at a rate of 100 Hz. All collected data were precisely time-space aligned with the IMU measurements. Then, a classic maximum likelihood state estimator incorporated all ground truth and IMU measurements to estimate final ground truth orientations, positions, velocities, and the biases of the gyroscope and accelerometer.

This dataset provides estimated high-precision velocity and IMU sensor biases. Therefore, it is well suited for experimenting with our method. It enables us to test sensor error prediction and position estimates. The dataset was split into training set and test set following the same splitting strategy as in related works [14], [15], as shown in Table I. The ground truth data was aligned to the IMU timestamps by interpolation. Additionally, as [34] reported, the ground truth on the V1_01 sequence of EuRoC is not accurate in its orientation estimate. Thus, this sequence was not involved in our experiments.

2) TUM-VI: TUM-VI [7] is a more recent visual-inertial dataset. It was collected by a handheld device with a non-static start. The IMU data was logged by the Bosch BMI160 IMU at 200 Hz. The accurate 6D pose ground truth was collected using a MoCap OptiTrack Flex13 at 120 Hz. All data were accurately aligned with the IMU measurements.

TUM-VI differs from EuRoC in two points. First, this dataset only provides ground truth positions and orientations thus it is not applicable to methods that require the use of accurate accelerations, angular velocities, and velocities. Second, the BMI160 IMU was strictly calibrated using the global optimization method. Accordingly, the calibrated parameters of the IMU were provided and the IMU data was calibrated. This allows us to simulate uncalibrated IMU data based on the given parameters to increase the diversity of the dataset.

We synthesized the uncalibrated IMU data, i.e., $\boldsymbol{a}_{\text{uncali}}$ and $\boldsymbol{\omega}_{\text{uncali}}$, of TUM-VI based on the given parameters and the formulas in [7] as follows:

$$\boldsymbol{a}_{\text{uncali}} = \boldsymbol{M}_{\boldsymbol{a}}(\boldsymbol{a}_{\text{cali}} + \boldsymbol{b}_{\boldsymbol{a}}), \tag{27}$$

$$\boldsymbol{\omega}_{\text{uncali}} = \boldsymbol{M}_{\boldsymbol{\omega}}(\boldsymbol{\omega}_{\text{cali}} + \boldsymbol{b}_{\boldsymbol{\omega}}), \tag{28}$$

where $\boldsymbol{M}_{\boldsymbol{a}}$ and $\boldsymbol{M}_{\boldsymbol{\omega}}$ contain scale factors and axis-misalignment, $\boldsymbol{b}_{\boldsymbol{a}}$ and $\boldsymbol{b}_{\boldsymbol{\omega}}$ are zero biases, $\boldsymbol{a}_{\text{cali}}$ and $\boldsymbol{\omega}_{\text{cali}}$ are the calibrated IMU data provided by the TUM-VI. The dataset containing the synthesized IMU data is referred to as TUM-VI (Uncali) in our experiments. Correspondingly, the dataset containing the calibrated IMU data is dubbed TUM-VI (Cali). We took the six-room sequences of TUM-VI (Uncali) and TUM-VI (Cali) as the ground truth 6D poses are available over the whole trajectory. Similarly, the ground truth data was aligned to the IMU timestamps by interpolation and the dataset was split into a training set and test set, as shown in Table I.

TABLE I
TRAIN AND TEST SEQUENCES.

Dataset	Train sequences [length]	(No.) Test sequences [length]
EuRoC	MH_01_easy [182 s] MH_03_medium [150 s] MH_05_difficult [111 s] V1_02_medium [83.5 s] V2_01_easy [112 s] V2_03_difficult [115 s]	(1) MH_02_easy [150 s] (2) MH_04_difficult [99 s] (3) V1_03_difficult [105 s] (4) V2_02_medium [115 s]
TUM-VI (Uncali)	room1 [140 s] room3 [140 s] room5 [141 s]	(5) room2 [143 s] (6) room4 [111 s] (7) room6 [130 s]
TUM-VI (Cali)	room1 [140 s] room3 [140 s] room5 [141 s]	(8) room2 [143 s] (9) room4 [111 s] (10) room6 [130 s]

B. Method Implementation

Our method was implemented based on PyTorch 1.13. The training process used an Adam optimizer [35] with 0.01 initial learning rate and 0.1 weight decay, which was adjusted using a cosine annealing schedule [36]. We empirically set the window size in loss function $T = 64$ with the IMU frequency of 200 Hz (see Section IV-F for details). Setting T to a power of 2 allows a faster computation of the loss function by concatenating the multiplications [14]. We trained the model for 1500 epochs using an NVIDIA TITAN RTX GPU, which took about 1 min with 8 min training data. In the test, predicting the calibrated IMU data takes $0.24\ \mu s$ per IMU measurement. We ran our method ten times with the same setting and then took the mean results.

C. Evaluation of Sensor Error Reduction

Our model aims to predict and compensate for the IMU sensor error. Thus, we compared the raw sensor error $\boldsymbol{\varepsilon}_a$, $\boldsymbol{\varepsilon}_g$ with the compensated sensor error $\boldsymbol{\varepsilon}_a - \hat{\boldsymbol{\varepsilon}}_a$ and $\boldsymbol{\varepsilon}_g - \hat{\boldsymbol{\varepsilon}}_g$ to evaluate whether our method correctly predicted and reduced the errors. Note that we only compared the residuals between the before and after calibration sensor data and ground truth inertial data. This is because the output of the data-driven calibration model does not explicitly distinguish between various types of sensor errors and is not directly related to the underlying IMU physical characteristics [27].

According to the sensor error model (8), we computed the raw error at time step i as

$$\begin{aligned} \boldsymbol{\varepsilon}_{a,i} &= \tilde{\boldsymbol{a}}_i - \hat{\boldsymbol{C}}_a^{-1}\boldsymbol{a}_i, \\ \boldsymbol{\varepsilon}_{g,i} &= \tilde{\boldsymbol{\omega}}_i - \hat{\boldsymbol{C}}_g^{-1}\boldsymbol{\omega}_i, \end{aligned} \tag{29}$$

where $\tilde{\boldsymbol{a}}_i$, $\tilde{\boldsymbol{\omega}}_i$ are the raw acceleration and angular velocity, respectively. $\hat{\boldsymbol{C}}_a^{-1}$ and $\hat{\boldsymbol{C}}_g^{-1}$ are the optimized scale factor and axis-misalignment for aligning the IMU data. $\boldsymbol{a}_i$ and $\boldsymbol{\omega}_i$ are the ideal IMU data derived from the interpolated ground truth velocity and orientation as

$$\boldsymbol{a}_i = \boldsymbol{R}_i^T\left(\frac{(\boldsymbol{v}_{i+1} - \boldsymbol{v}_i)}{\Delta t} - \boldsymbol{g}\right), \tag{30}$$

$$\boldsymbol{\omega}_i = \log_{SO3}(\boldsymbol{R}_i^T\boldsymbol{R}_{i+1})/\Delta t. \tag{31}$$

We computed the compensated sensor error $\boldsymbol{\varepsilon}_a - \hat{\boldsymbol{\varepsilon}}_a$ and $\boldsymbol{\varepsilon}_g - \hat{\boldsymbol{\varepsilon}}_g$ by removing the predicted error from the raw error. Then the remains were the sensor errors of our calibrated IMU data. We conducted this experiment only on EuRoC dataset as the high-precision velocities are available.

TABLE II
IMU SENSOR ERRORS ON EUROC TEST SEQUENCES,
ACCELERATION (IMPROVEMENT) [$\times 10^{-2} m/s^2$ (%)]/ANGULAR VELOCITY (IMPROVEMENT) [$\times 10^{-2} rad/s$ (%)].

	x-axis		y-axis		z-axis	
No.	$\varepsilon_a/\varepsilon_g$	$(\varepsilon_a - \hat{\varepsilon}_a)/(\varepsilon_g - \hat{\varepsilon}_g)$	$\varepsilon_a/\varepsilon_g$	$(\varepsilon_a - \hat{\varepsilon}_a)/(\varepsilon_g - \hat{\varepsilon}_g)$	$\varepsilon_a/\varepsilon_g$	$(\varepsilon_a - \hat{\varepsilon}_a)/(\varepsilon_g - \hat{\varepsilon}_g)$
1	0.40/0.26	0.24 (41%)/0.025 (90%)	6.30/2.11	0.39 (94%)/0.033 (98%)	0.44/7.71	0.13 (70%)/0.074 (99%)
2	3.52/0.22	1.02 (71%)/0.084 (61%)	1.69/2.10	0.29 (83%)/0.247 (88%)	2.47/7.67	0.88 (64%)/0.233 (97%)
3	1.26/0.38	0.64 (49%)/0.073 (81%)	9.30/2.55	6.69 (28%)/0.243 (90%)	1.04/7.70	0.11 (89%)/0.123 (98%)
4	2.75/0.13	0.38 (86%)/0.076 (42%)	3.31/2.48	6.50 (-96%)/0.120 (95%)	3.45/7.86	1.81 (47%)/0.076 (99%)
average improvement:	62%/69%		27%/93%		67%/98%	

Errors were averaged on each axis to eliminate the noise effect. All values are shown in absolute terms.
The improvement (%) of x relative to $y = 1 - \frac{x}{y}$, the computation is the same for the other parts in the paper.

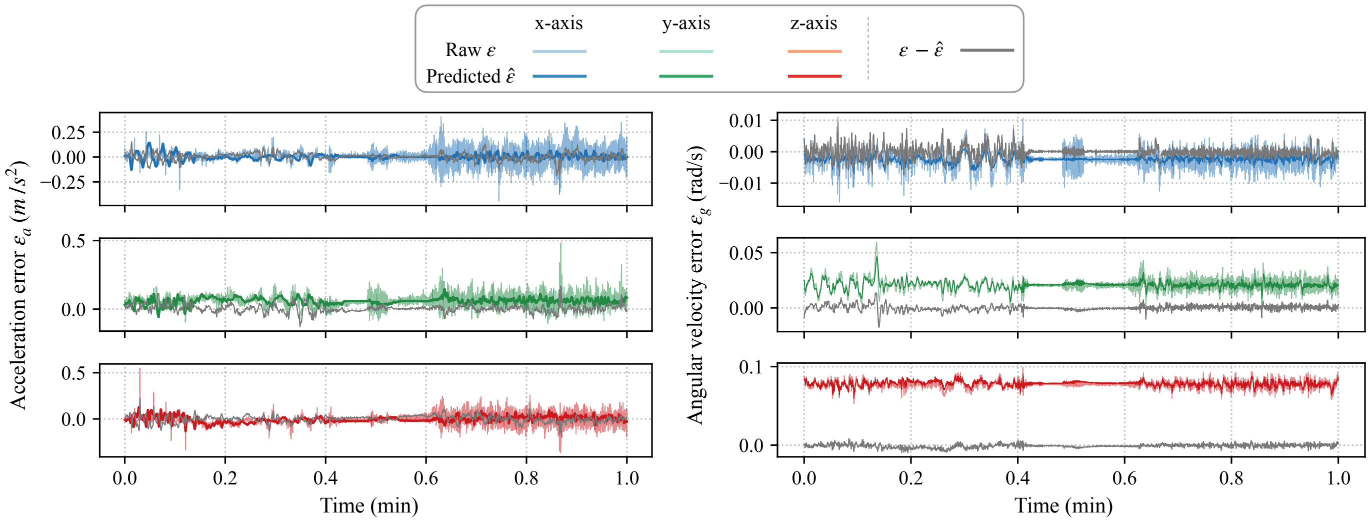

Fig. 3. Predicted error of accelerometer (left) and gyroscope (right) of test sequence EuRoC-MH_02_easy. All data were averaged every ten samples. The predicted error has the same trend as the raw error.

Table II shows the sensor error comparison results. For each sequence, we averaged the error on each axis to eliminate the noise influence. We show that our method removed the accelerometer and gyroscope errors by an average of 52% and 86%, respectively. Figure 3 shows the comparison of raw errors and our predicted errors on one test sequence. For the accelerometers, we were unable to predict high-frequency large noise errors. However, our predicted errors had the same trend as the raw errors, which indicates that our method eliminates the major low-frequency errors. Similarly, for the gyroscope with lower noise, low-frequency errors were predicted while high-frequency noise errors remained. Figure 4 illustrates the comparison of raw and our calibrated angular velocities for one test sequence. Our method shifted the signal slightly, which is visually hard to notice. However, the errors were reduced by more than 60%.

D. Evaluation of Calibration Effect for Inertial-based Odometry

The evaluation of the velocity, orientation, and position that are calculated from calibrated IMU data allows an intuitive perception of the change caused by the calibration. Thus, we inferred and evaluated these data from raw IMU data and calibrated IMU data using the kinematic motion model (3), (4), and (5).

1) Comparison of Orientation Estimates: We evaluated the orientation estimates using the following metrics:

- *Absolute Orientation Error (AOE)*: the root mean square error (RMSE) between the ground truth and inferred orientation for a whole trajectory sequence as

$$\mathrm{AOE} = \sqrt{\frac{1}{n}\sum_{i=1}^{n} ||\log_{SO3}(\boldsymbol{R}_i^T \hat{\boldsymbol{R}}_i)||_2^2}, \tag{32}$$

where $\boldsymbol{R}_i$ and $\hat{\boldsymbol{R}}_i$ denote the ground truth and inferred rotation matrices from the angular velocity at time step i through (3). $\log_{SO(3)}(\cdot)$ is the $SO(3)$ logarithm map.

- *Absolute Yaw Error (AYE)*: the RMSE between the ground truth and inferred yaw error for a whole trajectory sequence as

$$\mathrm{AYE} = \sqrt{\frac{1}{n}\sum_{i=1}^{n} ||\gamma_i - \hat{\gamma}_i||_2^2}, \tag{33}$$

where γ_i and $\hat{\gamma}_i$ denote the ground truth and inferred yaw at time step i. We measure AYE for comparison with the

TABLE III
ABSOLUTE ORIENTATION ERROR/ABSOLUTE YAW ERROR (IMPROVEMENT) [DEG/DEG (%)] ON EUROC TEST SEQUENCES.

		Huang *et al.*[1]		Buchanan *et al.*[2]		DUET[1]	
No.	Madgwick *et al.*	Baseline*	Method	Baseline*	Method	Baseline*	Method
1	115.11/44.07	-/0.67	-/1.35 (-101%)	3.21/-	2.86 (11%)/-	6.20/5.17	4.78 (**23**%)/3.43 (**34**%)
2	100.04/41.67	-/1.02	-/1.19 (-17%)	0.89/-	0.76 (**15**%)/-	1.46/1.13	1.96 (-34%)/1.29 (**-14**%)
3	85.25/29.46	-/1.80	-/1.00 (**44**%)	4.78/-	1.87 (**61**%)/-	1.91/1.28	1.73 (9%)/1.12 (13%)
4	110.74/42.20	-/1.94	-/1.63 (16%)	3.78/-	1.31 (**65**%)/-	3.86/3.02	3.66 (5%)/1.57 (**48**%)

[1] Integration from IMU data only.
[2] Fusion with visual features.
* All baselines are Brossard *et al.*, but were evaluated in different ways.

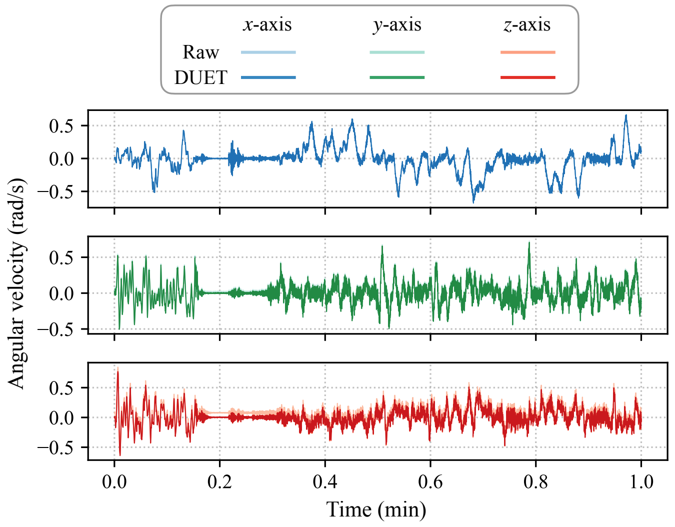

Fig. 4. Raw and deep calibrated angular velocity of test sequence EuRoC-MH_04_difficult. Our method removed the slight drift from raw angular velocity.

TABLE IV
ABSOLUTE ORIENTATION ERROR UNCALIB/CALIB [DEG/DEG] ON TUM-VI TEST SEQUENCES.

No.	Madgwick *et al.*	Brossard *et al.*	DUET
5/8	115.44/14.45	15.45/2.49	**1.77/1.72**
6/9	59.11/3.55	18.70/**0.99**	**1.12**/1.09
7/10	104.80/5.37	20.02/2.02	**2.05/1.91**

competing method Huang *et al.* [15] as it only reported this metric.

In terms of the orientation estimates, the closest works to ours are Brossard *et al.* [14], Huang *et al.* [15], and Buchanan *et al.* [20]. For the EuRoC dataset, we ran Brossard *et al.* ten times with the same setting using the source code they provided, then took the average results as the baseline for the comparison. Huang *et al.* and Buchanan *et al.* also used the results of Brossard *et al.* as baselines. However, the baselines were evaluated in different environments and metrics. Thus, we used the results provided in their papers directly and show relative improvement for comparison. Note that Huang *et al.* only reported AYE while Buchanan *et al.* reported AOE. For better comparison, we reported both. In addition, we calculated the AOE and AYE resulting from the Madgwick orientation filter [37] for comparison with traditional filter-based methods. For TUM-VI (Uncali) and TUM-VI (Cali), we compared with Madgwick *et al.* and Brossard *et al.* that used the same evaluation strategy as on EuRoC.

Table III summarizes the results on EuRoC. Overall, errors of learning-based methods are smaller than that of the traditional IMU-only filtering-based method, which is consistent with the findings in OriNet [16]. In terms of absolute yaw error, we slightly outperformed Huang *et al.*, even though they use a more sophisticated TCN network structure. However, in the case of AOE, Buchanan *et al.* is better than ours. There are two reasons for this. First, they directly use ground truth bias for learning and prediction. This allows them to learn pure biases of the gyroscope without any external impact. However, we use orientation for model learning, which is more practical but is affected by noise and dynamic motion. Second, the results may have been caused by network differences because they use a more sophisticated Transformer network, while we use the basic CNN network. Note that in this work, instead of using complex networks and optimizing network parameters to improve performance, we focus on a more general and practical framework for deep IMU calibration from dynamic high-precision motion data for inertial-based odometry.

Table IV shows the AOE on uncalibrated and calibrated TUM-VI dataset. For the synthesized uncalibrated sequences, we achieved an improvement of over 90% compared to the raw data and outperformed the Brossard *et al.* by 10% to 20%. This indicates that our method can remove the gyroscope sensor error and improve the accuracy of orientation estimates. Even for calibrated sequences, our method achieved an improvement of more than 50% in orientation estimates and was comparable to that of Brossard *et al.*

2) Comparison of Velocity Estimates: We evaluated the performance of calibrated acceleration by comparing the inferred velocity with that of raw acceleration using the absolute velocity error (AVE), which is defined as:

$$\mathrm{AVE} = \sqrt{\frac{1}{n}\sum_{i=1}^{n} ||\boldsymbol{v}_i - \hat{\boldsymbol{v}}_i||_2^2}, \tag{34}$$

where $\boldsymbol{v}_i$ denotes the ground truth velocity at time step i, and $\hat{\boldsymbol{v}}_i$ is the velocity computed through (4) from the acceleration. To eliminate the impact of orientation errors, we rotated the acceleration using the ground truth orientation. We only

TABLE V
ABSOLUTE VELOCITY ERROR AND IMPROVEMENT [m/s (%)] ON EUROC TEST SEQUENCES.

No.	Raw	MSE	DUET
1	11.66	11.26 (3%)	0.76 (**93%**)
2	6.85	2.85 (58%)	0.99 (**86%**)
3	4.88	0.62 (**87%**)	1.02 (79%)
4	7.20	3.52 (**51%**)	3.51 (**51%**)

measured the AVE on EuRoC dataset as they provided the accurate velocity ground truth. In addition, we replaced our loss function using mean square error (MSE) and trained using the ideal acceleration that was derived from the interpolated ground truth velocity and orientation through (30). This follows the same idea as in [21].

Table V summarizes the AVE on EuRoC test sequences. Compared to the results from the raw acceleration, we improved the accuracy by more than 50% on all test sequences. Besides, we reduced the error to nearly 1 m/s on three of the test sequences. Compared to the results based on the MSE loss function, we achieved comparable results that were more robust. This demonstrates that our proposed position-based loss function not only achieves a similar effect as based on ground truth acceleration, but also effectively avoids network overfitting and being affected by anomalous acceleration.

Although accelerometer calibration can be achieved on the basis of ground truth acceleration, in practice it is difficult to obtain relatively accurate acceleration using only high-precision pose tracking devices. Current studies [19] typically extrapolate this information solely from ground truth positions and orientations as

$$\boldsymbol{a}_i = \frac{\boldsymbol{p}_{i+1} - 2\boldsymbol{p}_i + \boldsymbol{p}_{i-1}}{\Delta t^2}. \tag{35}$$

However, this derivation is impaired in practice by the position jitter of the tracking system. As shown in Figure 5, the derived acceleration changed abruptly and had higher noise than the raw acceleration, due to sharp fluctuations in the position ground truth. Therefore, our proposed position-based method is more flexible and robust than methods based on accelerations and angular velocities.

3) Comparison of Position Estimates via Inertial-only Odometry: Position estimates are the most relevant indicator for inertial-based odometry. Thus, we inferred the position from calibrated IMU data using the kinematic motion model used in inertial-based odometry. Then we compared the results with that of raw IMU data. We also compared the results from IMU data calibrated for the gyroscope only to evaluate the effect of calibrating for both the gyroscope and the accelerometer. To evaluate the accumulated error of inertial-only odometry, we used the relative translation error (RTE), which is computed as follows:

$$\text{RTE} = \frac{1}{m}\sum_{i=1}^{m}\sqrt{\frac{1}{n}\sum_{j=1}^{n}||\hat{\boldsymbol{p}}_{j,T'} - \boldsymbol{p}_{j,T'}||_2^2}, \tag{36}$$

where $\boldsymbol{p}$ and $\hat{\boldsymbol{p}}$ are the ground truth position and the estimated position, respectively. n is the number of samples during

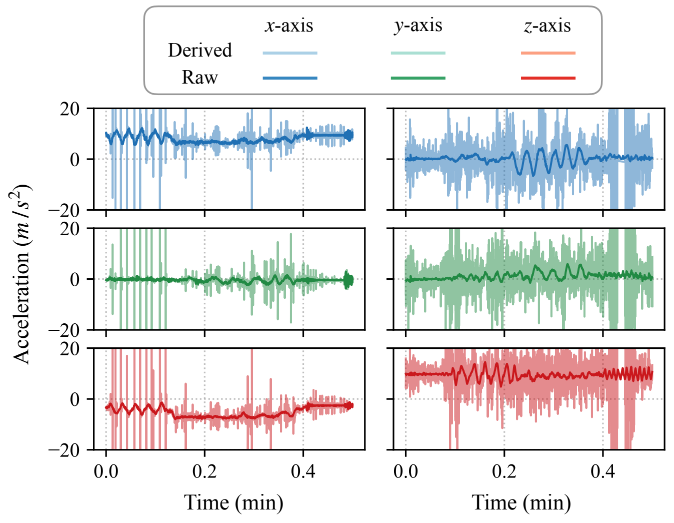

Fig. 5. Comparison of raw acceleration and derived acceleration from ground truth positions and orientations of EuRoC MH_02_easy (left) and TUM-VI Cali Room2 (right). The derived acceleration suffered from position fluctuation.

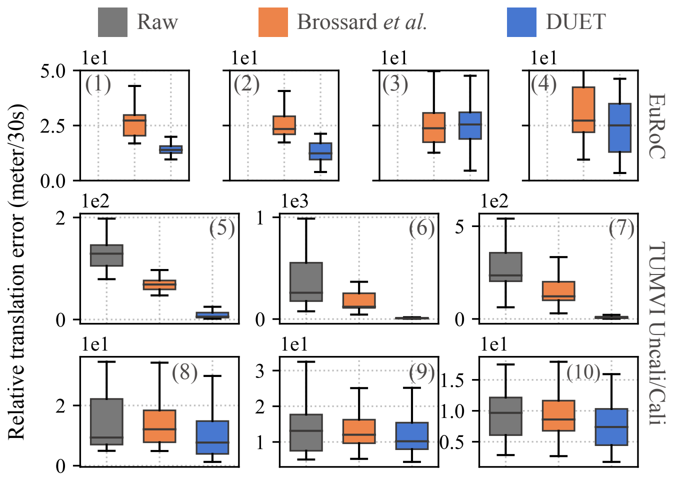

Fig. 6. Relative Translation Error (RTE) in 30 s on the test sequences of EuRoC (top), TUM-VI Uncali (middle), and TUM-VI Cali (bottom). Our method significantly reduced the accumulated error on the sequences that use uncalibrated IMU while slightly improved the accuracy on the sequences that use calibrated IMU.

a duration window T'. We randomly chose m segments of length T', computed the estimated position from a ground truth start, and then averaged the results. RTE is more suitable than absolute translation error for evaluating inertial-only odometry because it excludes the influence of sequence length on the results and focuses only on the accumulated error over a specific duration. We set $m = 50$, $T' = 30s$ in our experiments.

As shown in Figure 6, the position estimates were unreliable on EuRoC and TUM-VI (Uncali) datasets, in which the IMUs were uncalibrated. In contrast, our method reduced the position error accumulated in 30 s by approximately 90%, when compared to that obtained from raw IMU data. Even compared

TABLE VI
ABSOLUTE TRANSLATION ERROR (M) ON ALL TEST SEQUENCES.

No.	Zhang *et al.* [18]	Buchanan *et al.* [20]	Raw	DUET	No.	Raw[1]	DUET	No.	Raw	DUET
1	0.15	0.13	0.084	**0.072** (14%)	5	-	**0.244**	8	**0.053**	0.122 (-130%)
2	0.14	0.25	0.131	**0.113** (14%)	6	-	**0.211**	9	**0.024**	0.084 (-250%)
3	**0.15**	0.17	0.194	0.165 (15%)	7	-	**0.156**	10	0.064	**0.063** (2%)
4	0.10	0.10	0.159	**0.095** (40%)						

[1] Vins-mono with raw IMU data failed in test sequence 5, 6, and 7.

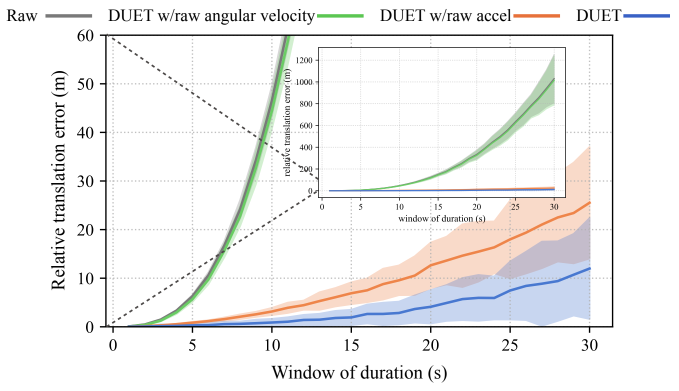

Fig. 7. Relative Translation Error (RTE) on test sequence MH_04_difficult of EuRoC dataset. The error from raw IMU data exponentially increased with time, while our method reduced the accumulated error to 10 m in 30 s.

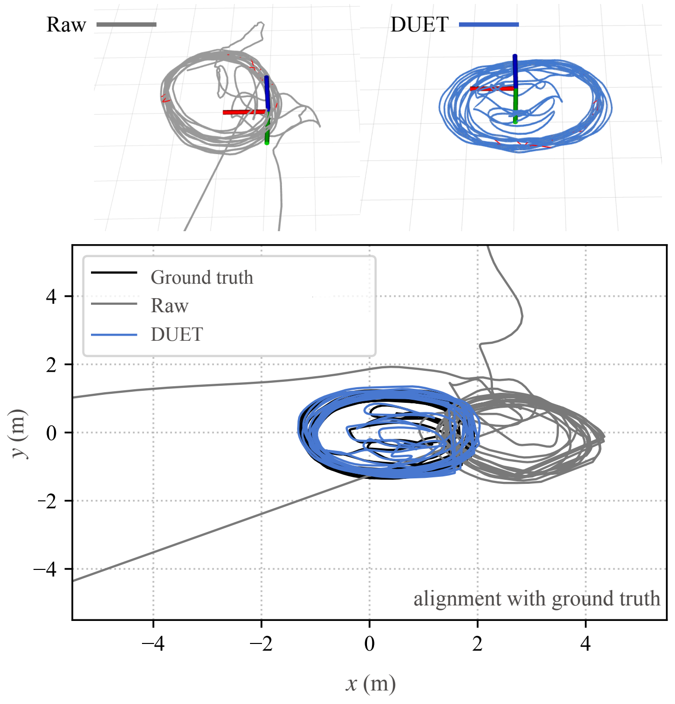

Fig. 8. VIO 3D (top) and horizontal (bottom) trajectories of TUM-VI Uncali Room 2 sequence. VIO with raw IMU failed when visual information was unstable. Our data-driven calibrated IMU data helped VIO overcome the unstable period and ensured continued odometry.

to the position estimates from the already well-calibrated IMU, we reduced the errors by at most 30%. Moreover, our accumulated errors were reduced by at least 20% compared to the errors of calibrated gyroscope only. This indicates that calibrating the gyroscope and accelerometer further reduces the error accumulation rate than calibrating the gyroscope only.

Figure 7 illustrates the error accumulation with time for one test sequence of EuRoC. The position errors from raw IMU data and IMU data measured only with accelerometer calibration increase exponentially with time, and exceed 1 km in 30 s. Our method slows down the rate of error accumulation and reduces the error to 10 m in 30 s. Compared to only gyroscope calibration, the error is reduced by more than 50%.

4) Comparison of Position Estimates via Visual-inertial Odometry: Data-driven IMU calibration is still being studied as a promising approach to improve the accuracy and robustness of VIO. As Zhang *et al.* [18] and Buchanan *et al.* [20] reported, the processed IMU data through data-driven methods improved the position estimate accuracy of VIO by at most 66%. In this work, we evaluated the position estimates from VINS-Mono [38] with raw IMU data and our calibrated IMU data to assess the impact of data-driven IMU calibration on VIO in different scenarios. Note that we only listed the results of competing methods but did not directly compare them because each method was based on a different VIO algorithm. We used the absolute translation error (ATE) to measure the performance, which is computed as

$$\text{ATE} = \sqrt{\frac{1}{n}\sum_{i=1}^{n} ||\hat{\boldsymbol{p}}_i - \boldsymbol{p}_i||_2^2}, \tag{37}$$

where n is the number of samples over a whole sequence.

Table VI shows the ATE on all test sequences. For EuRoC test sequences (No.1-4), our calibrated IMU data reduced the position estimates error by an average of 20%. This improvement is limited because the good visual conditions of these sequences allowed high accuracy of VIO. For TUM-VI Uncali test sequences (No.5-7), the VINS-Mono failed with raw IMU data. As shown in Figure 8, a dramatic position drift appears at the beginning of VIO with raw IMU trajectory. This is because TUM-VI does not start from a stationary state and the fast rotation challenging scenes are difficult to track accurately at the beginning, resulting in the IMU not being well calibrated in real-time. In contrast, our calibrated IMU helps VIO overcome the shaky start and ensure continued odometry. This indicates that our method can improve the robustness of VIO, especially for challenging visual situations. However, for TUM-VI Cali test sequences (No.8-10), our method was not able to further improve the calibrated IMU but had a negative effect on the position estimates accuracy of VIO. This is because performing data-driven calibration on the IMU data that has already been optimized using the global optimization method impairs the data and further leads to a reduction in the position estimate accuracy. This indicates that our method is not applicable to optimized and processed IMU data.

In Section IV-C, we showed that our method successfully predicted the low-frequency sensor errors and removed them from the raw gyroscope and accelerometer measurements. In Section IV-D1, Section IV-D2, and Section IV-D3, we conducted experiments in terms of IO and showed that our method reduces the orientation, velocity estimates errors as well as the error accumulation rate. We verified the feasibility of data-driven IMU calibration from high-precision tracking trajectory only, which is a promising method for calibrating IMU in VIO. To further explore the impact of our method on VIO, in Section IV-D4, we conducted experiments on three different scenarios. The results showed that: 1) for good visual conditions and uncalibrated IMU, our method slightly improves the position estimates accuracy; however, 2) for calibrated IMU, our method impairs the position estimates; 3) once visual information is temporarily unreliable, our method is an effective way to improve the robustness and accuracy of VIO.

E. Discussion on Impact of Bias Changes

We note that in Table II, the error reduction on the gyroscope is better than on the accelerometer. This is primarily due to the substantial changes in accelerometer errors, especially for the biases. This issue is also known as the generalization issue of data-driven approaches, i.e., trained on one domain and tested on another domain suffered from performance degradation [27]. Therefore, we provide experimental evaluation regarding the impact of bias changes on the data-driven model performance. We analyzed this impact by investigating provided biases of EuRoC sequences and performing further experiments through the training-test splitting of the data collected on different days.

As shown in Figure 9, we calculated the mean bias of each sequence in EuRoC. Overall, the biases of the acceleration vary considerably for each sequence. This has resulted in a general AVE improvement in the range of 80% to 90%, as shown in Table V. Notably, the acceleration biases of the V2_02_medium sequence in the x-axis and the y-axis were completely different from others. These can be considered outlier patterns for the data-driven model, resulting in only a 51% improvement in AVE. In contrast, the changes in biases for angular velocity are more minor than those for acceleration. As such, the AOE has more than 90% improvement on all test sequences.

TABLE VII
ERRORS AND IMPROVEMENT (AOE: [DEG (%)], AVE: [m/s (%)]) ON EUROC TEST SEQUENCES.

Test seq.	AOE (Madgwick *et al.*/DUET)	AVE (Raw/DUET)
V1_02_medium	76.81/1.91 (98%)	2.56/1.64 (36%)
V1_03_difficult	85.25/1.34 (98%)	4.88/0.63 (87%)
V2_01_easy	111.92/8.73 (92%)	9.25/5.32 (42%)
V2_02_medium	110.74/5.34 (95%)	7.20/3.33 (54%)
V2_03_difficult	92.92/4.59 (95%)	5.89/7.15 (-21%)

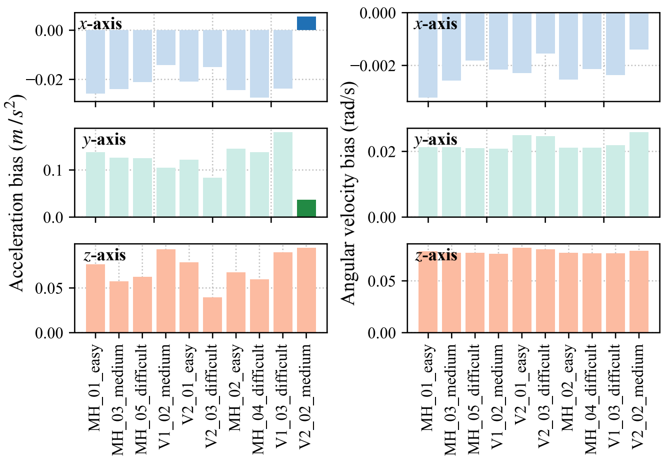

Fig. 9. Biases of acceleration (left) and angular velocity (right) for each sequence of EuRoC. The ground truth biases were estimated by fusing IMU measurements and high-precision tracking data. We take the mean bias of each sequence and each axis.

The low-cost MEMS IMU errors vary with time. To further validate the impact of error changes on model performance, we split the EuRoC into training and test data according to the data collection time, i.e., five MH sequences collected on the same day into training data and five V(icon) sequences into test data. Among the five test sequences, V1_02 and V1_03 were collected one day after the collection of MH sequences, and the other three test sequences were collected four months later.

A similar finding is evidenced by the results in Table VII. The model consistently performs above 90% in reducing the AOE where the bias changes among all sequences are not substantial. Nevertheless, the performance still degraded by about 5% on the test sequences collected four months later. As for the acceleration error mitigation, the model performance has degraded due to the large magnitude of bias changes. The average AVE improvement in the first four test sequences is 55%, ranging from 36% to 87%. On the V2_03, the completely different biases on all three axes result in a negative improvement on the AVE.

The generalization problem is always a major challenge for deep learning methods. Further experiments have shown that large differences between training and test data patterns lead to model performance degradation, which confirms the challenges summarized in the previous work [27], [39]. We now provide two points that we consider useful to solve this issue and push the model into practice in the future: 1) the current proposed method does not take into account the factors that will significantly affect the errors such as temperature, dynamic forces, etc. The integration of these variables into the data-driven model may improve the adaptability of the model to different scenarios; 2) it may prove helpful to integrate the current framework with potential online adaptation learning strategies, such as few-shot learning and test-time optimiza-

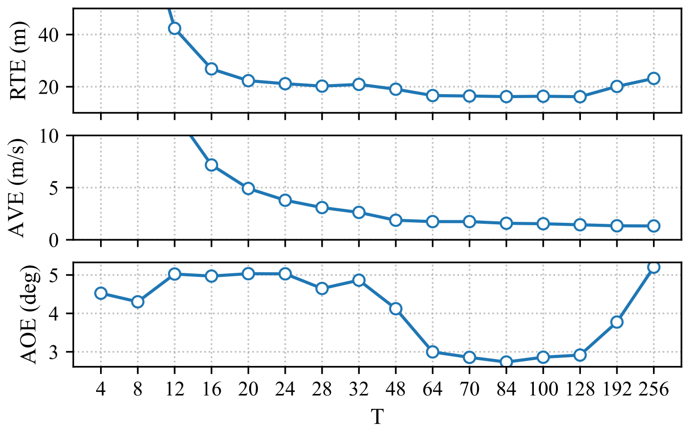

(a) Error trend with respect to T.

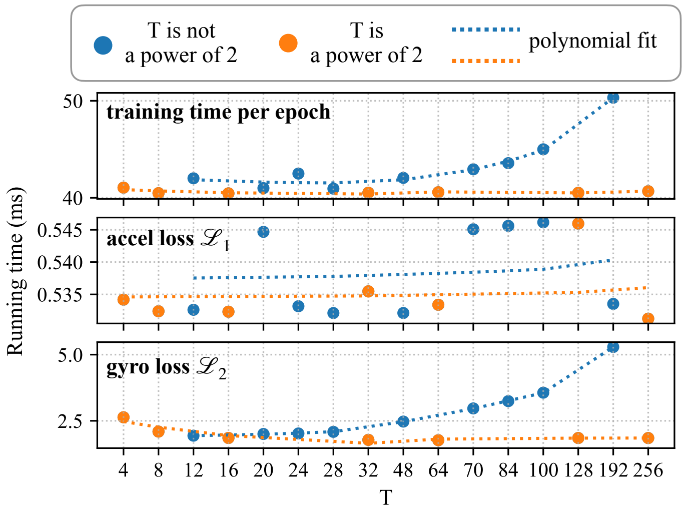

(b) Running time trend with respect to T.

Fig. 10. The effect of T on (a) model performance; and (b) training time. As T increases, RTE and AVE decrease and stabilize until T reaches 64. AOE is lower when T lies between 64 and 128. The running time increases with T, which is mainly caused by the increased computation time of $\mathcal{L}_2$.

tion.

F. Discussion on Choice of T

In our loss function, T is a key hyperparameter because it affects the effectiveness of model learning and training time complexity. Thus, we emphasize a few important points to choose a proper T successfully. We evaluated the effect of different T on the training time and the mode performance on the EuRoC dataset, respectively.

As shown in Figure 10a, as T increases, RTE and AVE decrease and stabilize when T reaches 64. This exhibits the negative effect of position jitter on model training when T is small, e.g., $T = 4$, and verifies that increasing T mitigates this effect effectively. However, AOE increases as T continues to increase, e.g., from 128 to 256. This is because our loss function aims to minimize the error of accumulated values within T windows, and an overly large T, that is, a large window size, would be detrimental to learning local error patterns and thus reduces the accuracy. This type of variation is similar to a low-pass filter in that a suitable value is chosen to reduce high-frequency noise and ensure that the necessary information is not lost.

Figure 10b illustrates the 1) training time per epoch; 2) computation time of $\mathcal{L}_1$; 3) computation time of $\mathcal{L}_2$ with respect to T. As T increases, the total training time increases, which is mainly caused by the increased computation time of $\mathcal{L}_2$. We compute the accumulated orientation within each window in parallel. Thus, the larger T is, the more rotation matrices need to be multiplied within each window. However, by computing two adjacent cumulative orientations in parallel within each window, the time complexity of $\mathcal{L}_2$ can be reduced from $O(T)$ to $O(\log(T))$ when T is an exponent of 2 [14]. Therefore, as shown in Figure 10b, the running time does not increase noticeably when T is a power of 2. We note that T does not affect the computation time of $\mathcal{L}_1$. In calculating $\mathcal{L}_1$, we first rotate all accelerations into the fixed world frame, then divide them according to the window size T and sum up accelerations within each window. Because T has a negligible impact on the computation time of the summation and the acceleration rotation is independent of T, the computation time of $\mathcal{L}_1$ does not vary with T.

The choice of T depends on the extent of the jitter in the ground truth motion data of the training set. Also, while guaranteeing the performance of the trained model, a smaller T can shorten the training time.

V. Conclusion and Limitations

We present a deep data-driven IMU calibration method for learning and compensating for sensor errors. The learning model is designed by fully considering the sensor error and kinematic motion models. This allows our method to learn the sensor error solely from high-precision positions and orientations. Compared with similar learning-based methods, our proposed method is more generally practical and straightforward because it does not require additional sensors and data processing techniques for the captured data to learn the calibration model. By compensating for run-time sensor errors, our method reduces the IO error accumulation rate, which we demonstrated with comprehensive experiments on two public VIO datasets. We show that our method reduces the absolute translation error of the baseline VIO method by 20% on average in scenarios with good visual information and ensures consistent odometry in unstable visual conditions.

Though learning-based methods have been shown to outperform traditional methods in some cases, there are still challenges in their deployment in real-world scenarios. For example, performance degradation in real-world applications may occur due to significant data gaps and sudden outliers. Traditional methods, on the contrary, still possess unique advantages in these situations. Future work should address how an integration of the strengths of both approaches would push the state of the art even further.

Acknowledgements

This work was supported in part by JSPS KAKENHI Grant Number JP20K11891.

References

[1] S. Adhikary and A. Ghosh, "E-BMI: A gait based smart remote BMI monitoring framework implementing edge computing and incremental machine learning," *Smart Health*, vol. 24, p. 100277, Jun. 2022.

[2] ——, "Dynamic time warping approach for optimized locomotor impairment detection using biomedical signal processing," *Biomedical Signal Processing and Control*, vol. 72, p. 103321, Feb. 2022.

[3] E. Marchand, H. Uchiyama, and F. Spindler, "Pose Estimation for Augmented Reality: A Hands-On Survey," *IEEE Transactions on Visualization and Computer Graphics*, vol. 22, no. 12, pp. 2633–2651, Dec. 2016.

[4] T. Taketomi, H. Uchiyama, and S. Ikeda, "Visual SLAM algorithms: A survey from 2010 to 2016," *IPSJ Transactions on Computer Vision and Applications*, vol. 9, no. 1, p. 16, Jun. 2017.

[5] S. Herath, H. Yan, and Y. Furukawa, "RoNIN: Robust Neural Inertial Navigation in the Wild: Benchmark, Evaluations, amp; New Methods," in *2020 IEEE International Conference on Robotics and Automation (ICRA)*, May 2020, pp. 3146–3152.

[6] M. Servières, V. Renaudin, A. Dupuis, and N. Antigny, "Visual and Visual-Inertial SLAM: State of the Art, Classification, and Experimental Benchmarking," *Journal of Sensors*, vol. 2021, p. e2054828, Feb. 2021.

[7] D. Schubert, T. Goll, N. Demmel, V. Usenko, J. Stückler, and D. Cremers, "The TUM VI Benchmark for Evaluating Visual-Inertial Odometry," in *2018 IEEE/RSJ International Conference on Intelligent Robots and Systems (IROS)*, Oct. 2018, pp. 1680–1687.

[8] X. Ru, N. Gu, H. Shang, and H. Zhang, "MEMS Inertial Sensor Calibration Technology: Current Status and Future Trends," *Micromachines*, vol. 13, no. 6, p. 879, Jun. 2022.

[9] D. Tedaldi, A. Pretto, and E. Menegatti, "A robust and easy to implement method for imu calibration without external equipments," in *2014 IEEE International Conference on Robotics and Automation (ICRA)*. IEEE, 2014, pp. 3042–3049.

[10] L. Ye, Y. Guo, and S. W. Su, "An Efficient Autocalibration Method for Triaxial Accelerometer," *IEEE Transactions on Instrumentation and Measurement*, vol. 66, no. 9, pp. 2380–2390, Sep. 2017.

[11] S.-h. P. Won and F. Golnaraghi, "A Triaxial Accelerometer Calibration Method Using a Mathematical Model," *IEEE Transactions on Instrumentation and Measurement*, vol. 59, no. 8, pp. 2144–2153, Aug. 2010.

[12] I. Frosio, F. Pedersini, and N. A. Borghese, "Autocalibration of MEMS Accelerometers," *IEEE Transactions on Instrumentation and Measurement*, vol. 58, no. 6, pp. 2034–2041, Jun. 2009.

[13] F. Ghanipoor, M. Hashemi, and H. Salarieh, "Toward Calibration of Low-Precision MEMS IMU Using a Nonlinear Model and TUKF," *IEEE Sensors Journal*, vol. 20, no. 8, pp. 4131–4138, Apr. 2020.

[14] M. Brossard, S. Bonnabel, and A. Barrau, "Denoising IMU Gyroscopes With Deep Learning for Open-Loop Attitude Estimation," *IEEE Robotics and Automation Letters*, vol. 5, no. 3, pp. 4796–4803, Jul. 2020.

[15] F. Huang, Z. Wang, L. Xing, and C. Gao, "A MEMS IMU Gyroscope Calibration Method Based on Deep Learning," *IEEE Transactions on Instrumentation and Measurement*, vol. 71, pp. 1–9, 2022.

[16] M. A. Esfahani, H. Wang, K. Wu, and S. Yuan, "Orinet: Robust 3-d orientation estimation with a single particular imu," *IEEE Robotics and Automation Letters*, vol. 5, no. 2, pp. 399–406, 2019.

[17] H. Chen, P. Aggarwal, T. M. Taha, and V. P. Chodavarapu, "Improving Inertial Sensor by Reducing Errors using Deep Learning Methodology," in *NAECON 2018 - IEEE National Aerospace and Electronics Conference*, Jul. 2018, pp. 197–202.

[18] M. Zhang, M. Zhang, Y. Chen, and M. Li, "IMU Data Processing For Inertial Aided Navigation: A Recurrent Neural Network Based Approach," in *2021 IEEE International Conference on Robotics and Automation (ICRA)*, May 2021, pp. 3992–3998.

[19] J. Steinbrener, C. Brommer, T. Jantos, A. Fornasier, and S. Weiss, "Improved State Propagation through AI-based Pre-processing and Downsampling of High-Speed Inertial Data," in *2022 International Conference on Robotics and Automation (ICRA)*, May 2022, pp. 6084–6090.

[20] R. Buchanan, V. Agrawal, M. Camurri, F. Dellaert, and M. Fallon, "Deep IMU Bias Inference for Robust Visual-Inertial Odometry With Factor Graphs," *IEEE Robotics and Automation Letters*, vol. 8, no. 1, pp. 41–48, Jan. 2023.

[21] D. Engelsman and I. Klein, "Data-Driven Denoising of Accelerometer Signals," *arXiv preprint arXiv:2206.05937*, Jun. 2022.

[22] S. Sun, D. Melamed, and K. Kitani, "IDOL: Inertial Deep Orientation-Estimation and Localization," *Proceedings of the AAAI Conference on Artificial Intelligence*, vol. 35, no. 7, pp. 6128–6137, May 2021.

[23] J. P. Silva do Monte Lima, H. Uchiyama, and R.-i. Taniguchi, "End-to-End Learning Framework for IMU-Based 6-DOF Odometry," *Sensors*, vol. 19, no. 17, p. 3777, Jan. 2019.

[24] C. Chen, C. X. Lu, J. Wahlström, A. Markham, and N. Trigoni, "Deep Neural Network Based Inertial Odometry Using Low-Cost Inertial Measurement Units," *IEEE Transactions on Mobile Computing*, vol. 20, no. 4, pp. 1351–1364, Apr. 2021.

[25] Q. A. Dugne-Hennequin, H. Uchiyama, and J. Paulo Silva Do Monte Lima, "Understanding the Behavior of Data-Driven Inertial Odometry With Kinematics-Mimicking Deep Neural Network," *IEEE Access*, vol. 9, pp. 36 589–36 619, 2021.

[26] W. Liu, D. Caruso, E. Ilg, J. Dong, A. I. Mourikis, K. Daniilidis, V. Kumar, and J. Engel, "TLIO: Tight Learned Inertial Odometry," *IEEE Robotics and Automation Letters*, vol. 5, no. 4, pp. 5653–5660, Oct. 2020.

[27] C. Chen, "Deep learning for inertial positioning: A survey," *arXiv preprint arXiv:2303.03757*, 2023.

[28] C. Jiang, S. Chen, Y. Chen, B. Zhang, Z. Feng, H. Zhou, and Y. Bo, "A MEMS IMU De-Noising Method Using Long Short Term Memory Recurrent Neural Networks (LSTM-RNN)," *Sensors*, vol. 18, no. 10, p. 3470, Oct. 2018.

[29] F. Yao, Z. Wu, Z. Wei, and D. Wang, "Few-shot Domain Adaptation for IMU Denoising," *arXiv preprint arXiv:2201.01537*, Mar. 2022.

[30] F. Yu and V. Koltun, "Multi-scale context aggregation by dilated convolutions," *arXiv preprint arXiv:1511.07122*, 2015.

[31] P. J. Huber, "Robust estimation of a location parameter," *Breakthroughs in statistics: Methodology and distribution*, pp. 492–518, 1992.

[32] A. Kendall, Y. Gal, and R. Cipolla, "Multi-Task Learning Using Uncertainty to Weigh Losses for Scene Geometry and Semantics," in *Proceedings of the IEEE Conference on Computer Vision and Pattern Recognition*, 2018, pp. 7482–7491.

[33] M. Burri, J. Nikolic, P. Gohl, T. Schneider, J. Rehder, S. Omari, M. W. Achtelik, and R. Siegwart, "The EuRoC micro aerial vehicle datasets," *The International Journal of Robotics Research*, vol. 35, no. 10, pp. 1157–1163, Sep. 2016.

[34] P. Geneva, K. Eckenhoff, W. Lee, Y. Yang, and G. Huang, "OpenVINS: A Research Platform for Visual-Inertial Estimation," in *2020 IEEE International Conference on Robotics and Automation (ICRA)*, May 2020, pp. 4666–4672.

[35] D. P. Kingma and J. Ba, "Adam: A Method for Stochastic Optimization," *arXiv preprint arXiv:1412.6980*, Dec. 2014.

[36] I. Loshchilov and F. Hutter, "SGDR: Stochastic Gradient Descent with Warm Restarts," *arXiv preprint arXiv:1608.03983*, 2016.

[37] S. O. H. Madgwick, A. J. L. Harrison, and R. Vaidyanathan, "Estimation of imu and marg orientation using a gradient descent algorithm," in *2011 IEEE International Conference on Rehabilitation Robotics*, 2011, pp. 1–7.

[38] T. Qin, P. Li, and S. Shen, "VINS-Mono: A Robust and Versatile Monocular Visual-Inertial State Estimator," *IEEE Transactions on Robotics*, vol. 34, no. 4, pp. 1004–1020, Aug. 2018.

[39] Y. Li, R. Chen, X. Niu, Y. Zhuang, Z. Gao, X. Hu, and N. El-Sheimy, "Inertial sensing meets machine learning: Opportunity or challenge?" *IEEE Transactions on Intelligent Transportation Systems*, vol. 23, no. 8, pp. 9995–10 011, 2022.